


Laser-Generated Ultrasonic Vortex in the Megahertz Frequency Range

Hui Zhou,^{1,2,‡} Ze-Ru Yang,^{1,2,‡} Qiu-Yu Li,^{1,2} Chao Zeng,^{1,2} Si-Yu Liu,^{1,2} Zhong-Hua Shen,^{1,2,†} and Wei-Wei Kan^{1,2,3,*}

¹*School of Science, Nanjing University of Science and Technology, Nanjing 210094, China*

²*MIIT Key Laboratory of Semiconductor Microstructure and Quantum Sensing, Nanjing University of Science and Technology, Nanjing 210094, China*

³*Key Laboratory of Modern Acoustics, MOE, Nanjing University, Nanjing 210094, China*

 (Received 17 April 2023; revised 20 July 2023; accepted 22 August 2023; published 11 September 2023)

Unlocking the full potential of wavefront manipulation and particle trapping with high spatial precision requires a flexible approach to remotely trigger the desired ultrasonic wave with high central frequency. In this work, we propose a scheme for generating ultrasonic vortices beyond 3 MHz through optoacoustic conversion with the tailored logarithmic spiral absorbing surface. By illuminating the light-absorbing surface with an 8-ns pulsed laser, the laser-generated ultrasonic waves from each loop of the spirals will coherently interfere with each other near their symmetric axis of propagation, and the vortex is then produced, with the common features of a helical wavefront and central null pressure. The generated vortex field with different topological charges is scanned in three dimensions with high spatial resolution using a parabolic focusing detection system. The proposed scheme can produce the desired vortex field at above 3.5 MHz without resorting to elaborate fabrication techniques or distributed arrays, and therefore, has potential in various fields, ranging from particle manipulation to other biomedical applications.

DOI: [10.1103/PhysRevApplied.20.034020](https://doi.org/10.1103/PhysRevApplied.20.034020)

I. INTRODUCTION

Ultrasound generated via optoacoustic effects exhibits the property of high central frequency [1,2] and broad bandwidth [3,4]. In recent years, various laser-based ultrasonic techniques have been of tremendous interest to researchers and industrial pioneers [5–9] and have been applied in ultrasound imaging [10,11] and precision therapy [12,13]. As there is no requirement for electrical connections, such optoacoustic transducers can be deposited on any surface for laser illumination [14], and the shape of this absorbing surface can be tailored for various applications [15,16]. With proper design, it is possible to generate different complex acoustic fields using such optoacoustic methods. As an intriguing complex field that carries orbital angular momentum, the acoustic vortex has been widely investigated [17–21] and sheds light on promising applications, such as particle manipulation [22,23] and other biomedical applications [24,25]. The typical characteristics of the vortex are the null-pressure magnitude at the core and helical dislocation of the wavefront. Notably, the helical dislocation is described by an azimuthal, θ , phase

dependence, $e^{im\theta}$, in which the number m is called the topological charge [26,27], corresponding to the order of the vortex, and thus, determining the total phase-accumulated variation in one full annular loop around the propagation axis.

The generation of the vortex field has become a crucial issue, owing to its broad application prospects [28,29]. In theory, the transducer array can generate the acoustic vortex boundlessly. Many studies have been conducted on this subject, and the features and application value of the vortex field generated with such methods have also been extensively and clearly demonstrated [30–33]. Recently, other methods have been explored for generating acoustic vortices in more cost-effective and flexible manners, including those based on acoustic metasurfaces [34–38]. The metasurface is a fantastic family of metastructures with the feature of subwavelength thickness and the capability of wavefront modulation by modifying the wave intensity and phase in a predefined manner [39,40]. Various structures, such as the Archimedean spiral [36], Fresnel spiral [37], and hybrid coiling slit [38], have been devised to transform the incident planar waves into vortices, of which the acoustic radiation force can be utilized for trapping particles [41]. To generate an ultrasonic vortex with robust performance when stimulated at different frequencies, multiarm coiling slits have been employed, and the

*kan@njjust.edu.cn

†shenzh@njjust.edu.cn

‡H. Zhou and Z. Yang contributed equally to this work.

resulting integer acoustic vortex has inherent broadband functionality [42]. Optoacoustic generation of a helicoidal ultrasonic beam with a center frequency of 750 kHz was also investigated and experimentally demonstrated previously [43]. Due to the demand for manipulation with high spatial resolution in practical applications, some pioneering research has been carried out toward acoustic vortices with higher frequencies [44–46]. The design methods for the vortex metasurface can be introduced into the scheme of optoacoustic excitation to form different types of ultrasonic vortex, then the high-frequency and broadband advantage of optoacoustic excitation can enable detection and manipulation with higher precision and resolution.

Here, we report the method of generating an ultrasonic vortex with comparatively high center frequency and controllable topological charge using a laser. The 8-ns pulsed laser irradiates the spiral absorbing surface to generate the vortex field. The parabolic focusing detection system is designed and constructed to scan the laser-generated high-frequency vortex field with fine spatial resolution. The experimental results show that the sustenance of the topological charge can be extended to a distance of several wavelengths in the propagation direction. Remarkably, the scheme has an intrinsic broadband and high-center-frequency feature due to the generation mechanism, which is of significance in practice. The generated acoustic vortices with different topological charges are presented, and agreement is observed between the predictions and experimental measurements. This study provides a compact solution to generate a broadband ultrasonic vortex in the multimegahertz-frequency range, without a complicated structure or electronic control system.

II. THEORY AND SIMULATION

Figure 1 shows a schematic diagram of optoacoustic generation. The light-absorbing material, like black dye or ink, is deposited on the transparent backing material in a spiral pattern, forming the optoacoustic conversion structure. As depicted in Fig. 1(a), the laser will transmit through the transparent backing and illuminate the light-absorbing layer, generating ultrasound waves according to the tailored pattern of deposition. Figure 1(b) displays the bottom view of the optoacoustic conversion surface with a spiral pattern for generating the acoustic vortex with $m = 1$. For simplicity, without loss of generality, here we consider the case of topological charge $m = 1$ to illustrate the working principle, and other types of vortex ultrasonic fields can be obtained using a similar approach. As shown in Fig. 1(c), the spiral region is enclosed by two logarithmic spiral curves, and the overall structural parameters of the two curves are expressed by the polar coordinates $r_1 = a_1 e^{b\theta}$ and $r_2 = a_2 e^{b\theta}$, with r and θ depicting the radial coordinate and the angular coordinate. The factors $a_1 =$

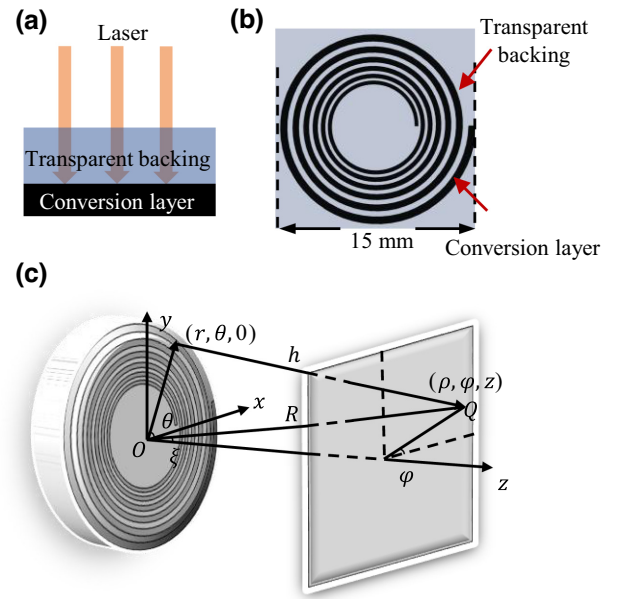


FIG. 1. (a) Side view of the vortex-generation device with the direction of laser incidence. (b) Bottom view. (c) Working principle of the spiral structure for generating ultrasonic vortices. Dark gray indicates the light-absorbing region.

2.76 mm and $a_2 = 2.97$ mm are the initial radii of the two spiral curves, and the azimuthal factor $b = 0.023$ determines the growth rate of rotation. The two spiral curves grow from $\theta_1 = 0$ to $\theta_2 = 12\pi$.

When this conversion layer is laser irradiated, the transient temperature change will trigger a rapid expansion nearby and generate acoustic waves in a coherent way towards the positive direction of the z axis, according to the deposited pattern of the absorbing material. The tailored spiral pattern here imposes helicity, rotating the phase of the generated waves and forming acoustic vortices by destructive interference around the z axis. For theoretical investigation of the laser-generated vortex in the frequency domain, the Rayleigh-Sommerfeld diffraction integral is utilized to calculate the acoustic pressure [42] at the observation point $Q(\rho, \varphi, z)$, where ρ and φ are, respectively, the radial and azimuthal coordinates at the observation plane, and z is the distance between the excitation surface and observation plane. The normalized pressure at the viewing point, Q , is governed by

$$P_m(\rho, \varphi, z) = \sum_{n=1}^m \int_{\theta_1}^{\theta_2} \int_{a_1 e^{b[\theta+2\pi(n-1)/m]}}^{a_2 e^{b[\theta+2\pi(n-1)/m]}} \frac{i\omega\rho_0}{2\pi h} e^{i(\omega t - kh)} r dr d\theta, \quad (1)$$

where m is the topological charge; ω and k are the angular frequency and wave number of the incident wave, respectively; ρ_0 is the mass density of the background

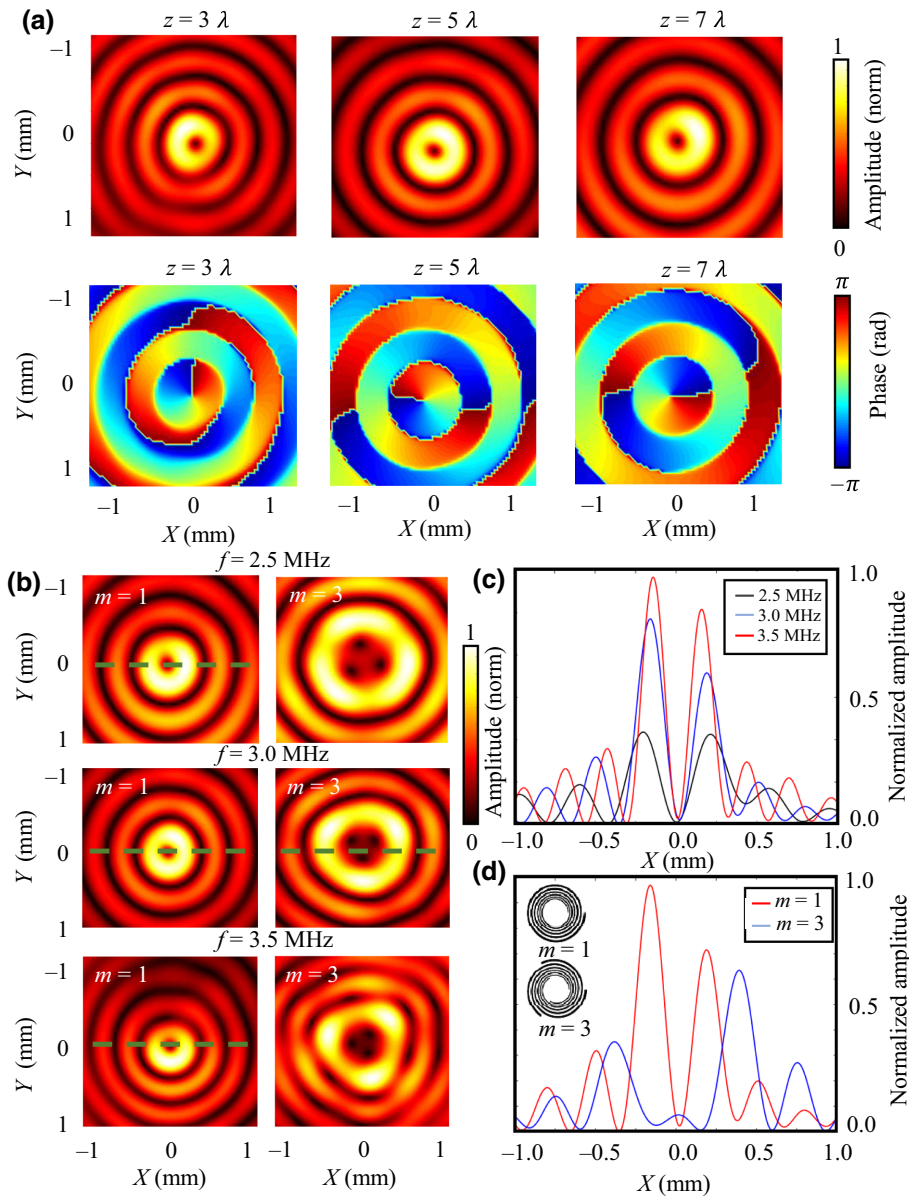


FIG. 2. (a) Acoustic pressure amplitude and phase distributions of the vortex acoustic field at three transverse planes, $z = 3\lambda$, 5λ , and 7λ ; topological charge $m = 1$; $f = 3$ MHz. (b) Amplitude distribution of the acoustic vortex in the x - y plane of different frequencies and topological charges, $z = 5\lambda$. (c) Amplitude distribution along the dashed lines, with different frequencies, $m = 1$, and (d) different topological charges, $f = 3$ MHz. Simulated using the k -wave toolbox [47].

material; $h = \sqrt{\rho^2 + r^2 + z^2 - 2rR \cos \varphi \sin \xi}$ is the distance between the viewing point and the point in the structure; $R = \sqrt{\rho^2 + z^2}$ is the distance between point Q and the origin point O ; and $\xi = \arctan(\rho/z)$ is the angle between point Q and the z axis. The vortex generated using this logarithmic spiral absorbing surface is also analyzed via numerical simulations, which agree well with the theoretical predictions. The theoretical calculated field distribution of the vortex with different topological charges is nearly the same as the simulation results obtained using the k -wave toolbox [14,47], as shown in Fig. 2. The simulation is performed on a $512 \times 512 \times 128$ grid, with a grid spacing of 0.03 mm in the x direction and y direction, and 0.06 mm in the z direction, where the z axis is the direction of sound propagation. The spiral absorbing surface is inserted at one end of the simulation domain

as a 512×512 source mask. The background medium is chosen to be water, the mass density and sound speed of which are 1000 kg/m^3 and 1500 m/s , respectively. The captured wave data at the sensor positions triggered by the broadband pulse are low-pass filtered at 6 MHz, and then transformed into the Harmonic field at each frequency by Fourier transformation. To verify the performance of the proposed spiral surface in maintaining the topological charge over a considerably long distance along the propagation direction, the simulation results of the optoacoustic vortex at varying distances are presented in Fig. 2(a). It can be observed that the acoustic pressure amplitude of the generated vortex field at different distances are distributed in a nearly ring-shaped pattern with a central null pressure. The phase changes by 2π in an annular loop, which is consistent with the characteristics of the vortex

field with a topological charge of 1. Meanwhile, the acoustic vortex diffuses with an increase in the distance, with the vortex central region slightly expanding during propagating. These results demonstrate that the logarithmic spiral absorbing surface is capable of exciting relatively stable vortex acoustic fields over a distance larger than 5λ .

Figure 2(b) illustrates the pressure-amplitude distribution of the vortex field at several different center frequencies and topological charges. The vortex feature of different frequencies generally has similar shapes; the number of vortex circles in the same range increases when increasing the frequency. Obviously, there are three phase singularities at the center with topological charge $m = 3$, and the range of the central null pressure increases. Figures 2(c) and 2(d) illustrate the acoustic-pressure-amplitude distribution along the dashed lines for varying frequencies and topological charges, respectively. The inset of Fig. 2(d) gives the logarithmic spiral patterns corresponding to acoustic vortices with topological charges $m = 1$ and $m = 3$. Parameter b is chosen to be 0.068 for $m = 3$, $\theta = 4\pi$, with a_1 and a_2 unchanged. It can be observed that the range of zero pressure at the center decreases with increasing frequency. In contrast, by increasing the topological charge, the range of zero pressure increases. In this sense, the target vortex field can be obtained by regulating the relevant parameters.

III. EXPERIMENTS

To validate the proposed optoacoustic generation method of the vortex acoustic field, the experimental setup is designed and established as schematically illustrated in Fig. 3(a). The optoacoustic device for generating the vortex is shown in Fig. 3(b). A pulsed laser (wavelength of 1064 nm, pulse width of 8 ns) is used to excite ultrasound

waves. The beam with a laser fluence of about 12.6 mJ/cm^2 illuminates the light-absorbing surface. Measurements of the vortex field are implemented using the semiparabolic focusing detection system, which consists of an aluminum semiparabolic reflector and a piezoelectric transducer with an aperture of 20 mm. The aluminum semiparabolic reflector is made for reflective focusing, allowing the generated high-frequency acoustic vortex to be scanned by the transducer with an aperture much larger than the wavelength. The configuration parameters of the parabolic reflector are designed according to the wavelength, the required angular spectrum, and the transducer aperture, and carefully aligned with the transducer for field scanning with high spatial resolution. The signals are recorded by an oscilloscope (PicoScope 5444D). The photodetector (DET10A, THORLABS, USA) is used to trigger the oscilloscope to start recording signals for time-synchronized measurements at different positions. During the process of acoustic detection, the stepping motor is used to control the movement of the detection system in three-dimensional space.

A photograph of the spiral absorbing surface for the acoustic vortex with $m = 1$ is given in Fig. 3(b). Many materials have been used as light-absorbing surfaces [16, 48], with high optoacoustic conversion efficiency and broadband characteristics. For our research objective of validating the method of optoacoustic vortex generation, we deposit a commonly used material, acrylic dye on a transparent polyvinyl chloride film, with a rubber stamp to form the optoacoustic conversion layer, without considering the further improvement of conversion efficiency. Some measures can be considered in a future study, such as using materials with a high coefficient of thermal expansion and better-absorbing materials to improve the optoacoustic conversion efficiency. The absorbing material

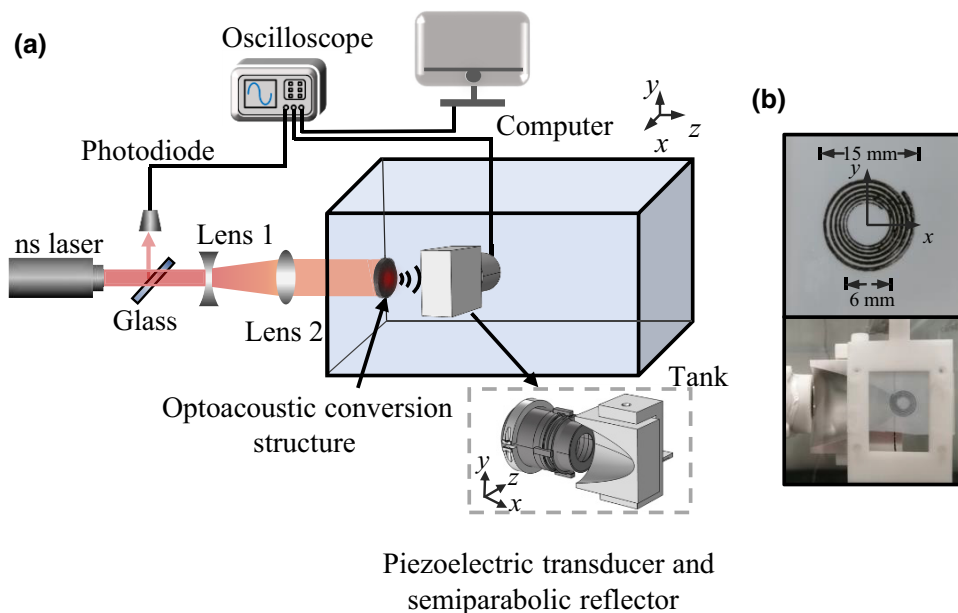


FIG. 3. (a) Schematic diagram of the experimental setup. (b) Photograph of the light-absorbing surface and the focusing detection system.

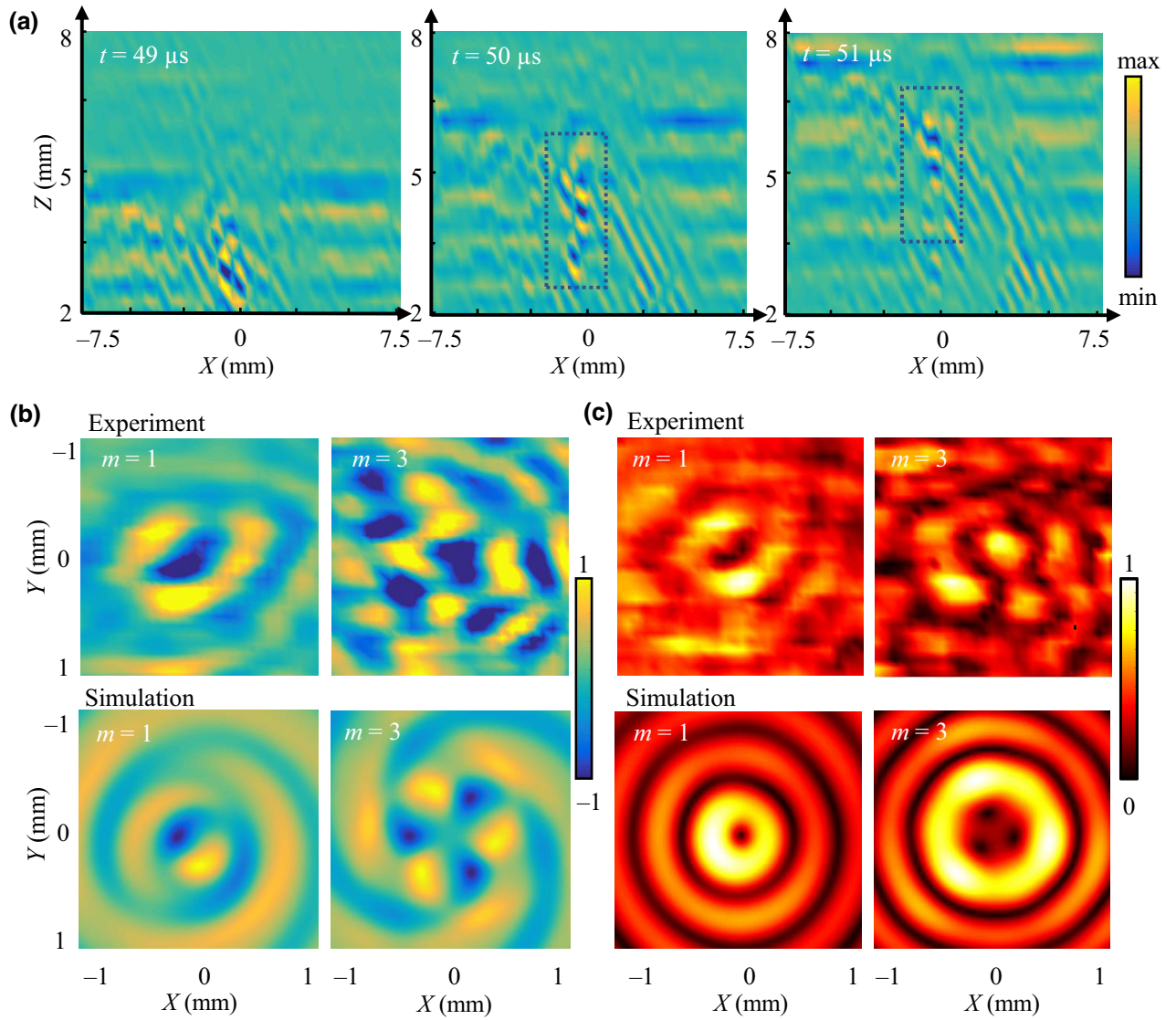


FIG. 4. (a) Measured transient acoustic field at $y = 0$. Comparison of experimental and simulation results of vortex acoustic field distribution in the x - y plane. (b) Transient wave field and (c) amplitude.

can also be transferred using a spiral aluminum masking template with the required spiral pattern hollowed out in the aluminum plate for a denser and more uniform pattern. Waterproof ink is also tested; this generates similar vortex fields, with only differences in the corresponding acoustic pressure amplitudes. The whole spiral area can be approximated as a circle with a radius of $r = 7.5$ mm. The initial radius of the spiral is about 2.76 mm, and the width of the spiral line gradually increases from 0.21 to 0.5 mm.

IV. RESULTS AND DISCUSSION

A. Acoustic wave propagation in the x - z plane

To analyze the distribution characteristics of the optoacoustic vortex field, the vortex field distribution in the x - z plane is recorded in the experiments. Figure 4(a) shows

the distribution of the transient field at different times in the x - z plane at $y = 0$. The scanning range in the x direction is set from $x = -7.5$ to 7.5 mm, corresponding to the size of the spiral region. In the z direction, the scanning range is set from $z = 2$ to 8 mm, where the value represents the distance between signal reception and excitation. The results indicate that the waves generated from the spiral region propagate forward; the wavelets generated by each spiral line are coherently superimposed and constantly form a new wavefront. Then, at $z = 3$ mm, the vortex gradually forms in the center of the scanned region. The dotted-line box in the figure marks the vortex field formed in the center.

By analyzing the acoustic field distribution of the vortex in the x - z plane, we can determine that the generated optoacoustic vortex can be observed at a distance of 3–6 mm

from the absorbing surface. In addition, according to the results of the x - z plane, it can also be determined that the central region of the vortex has a range of roughly 2 mm. The above analysis is beneficial for further capture of the acoustic vortex field in the x - y plane.

B. Experimental results for the generated vortex with different topological charges

For simplicity, without losing generality, we demonstrate the performance of the spiral absorbing surface with topological charges of $m = 1$ and $m = 3$ to show the feasibility and validity of the scheme. Figures 4(b) and 4(c) show the ultrasonic vortex field and the corresponding amplitude distribution in both experiments and simulations. The number of positive- and negative-pressure peaks of the vortices around the center both conform to their topological charges for $m = 1$ and $m = 3$, and the direction of rotation depends on the spiral direction of the absorbing surface. Similarly, the acoustic amplitude distribution exhibits an approximately annular distribution with a zero field at the center corresponding to the topological charge. The features of the experimentally observed

acoustic fields are in good agreement with the simulations. Although the distribution of the vortex field in the experiment is not perfect, the typical characteristics of a vortex can be clearly observed. The error may be caused by the uneven distribution of light-absorbing materials, or the spatial positioning error of the parabolic focusing detection setup. For all cases, the high-frequency broadband vortex acoustic fields can be effectively generated with the designed optoacoustic device and detected by the parabolic focusing detection system, thereby validating the proposed scheme.

C. Analysis of the generated ultrasonic vortex characteristics in both time and frequency domains

To further analyze the temporal and spectral characteristics of the optoacoustic vortex field, we investigate the transient acoustic field of vortices with a topological charge of $m = 1$ as it evolves over time. The experimentally measured transient vortex field in the x - y plane at $z = 5$ mm is illustrated in Fig. 5(a). The result shows that the generated vortex acoustic field exists approximately between 48 and 50 μ s, corresponding to the distance

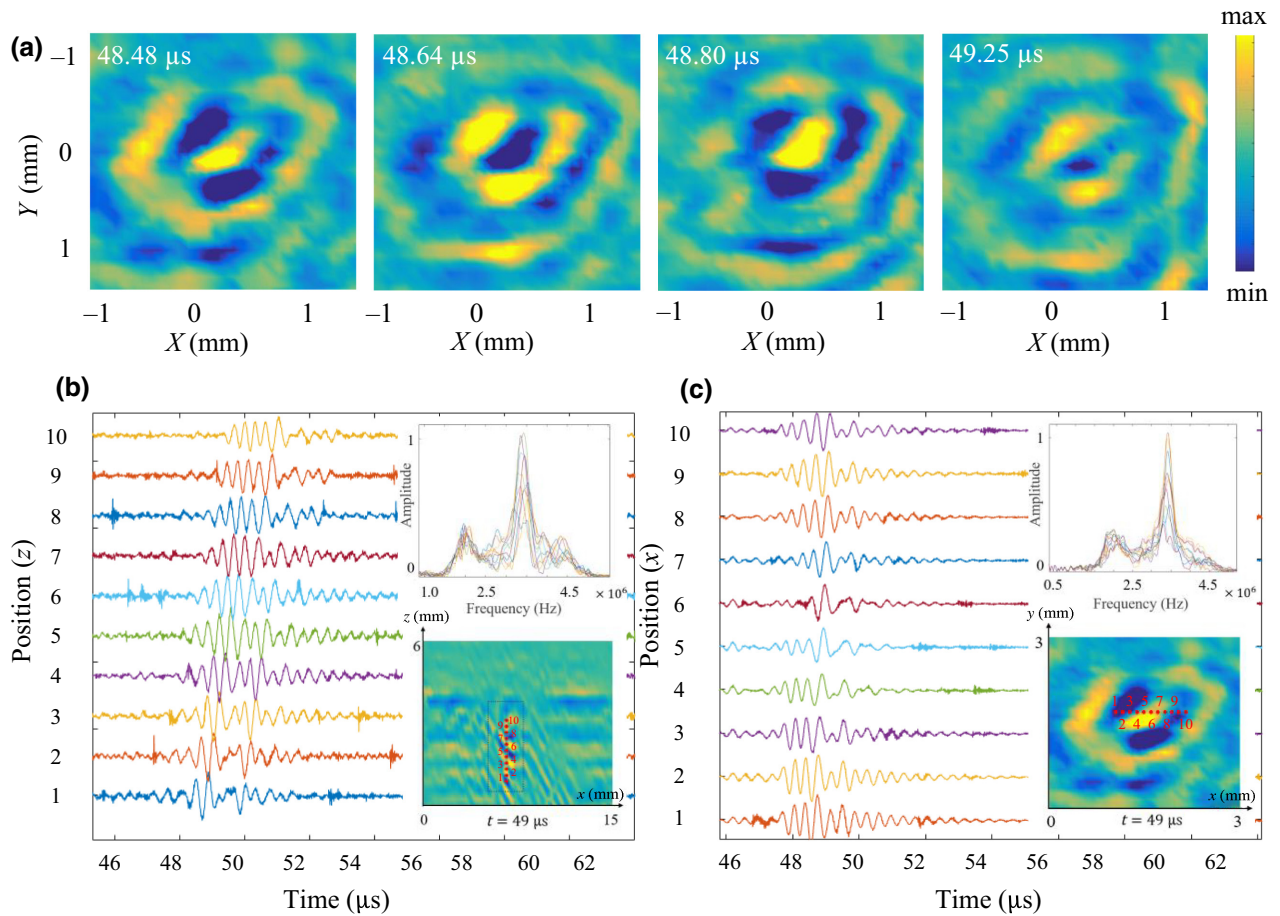


FIG. 5. (a) Experimental results of the acoustic field with $m = 1$ at the $z = 5$ mm plane. (b) Waveform and spectral diagram of the acoustic signals collected at different positions along the z direction and (c) along the x direction.

between excitation and detection, and the vortex field diffuses and gradually attenuates over time.

Figures 5(b) and 5(c) show the waveform and spectral diagram of the acoustic signals collected in the z and x directions of the vortex field. A total of 50×20 data points are collected in the x - z plane, of which 10 points around the vortex region along the z direction, as marked in red, are chosen to plot the transient ultrasonic waveforms, as shown in the inset of Fig. 5(b). By observing the waveform of the signal, it can be concluded that, as the distance of measurement increases beyond 5 times the wavelength, the emergence of the vortex signal is gradually delayed and the amplitude of the acoustic pressure gradually decreases. However, the waveform remains relatively unchanged, validating the robustness of this scheme.

Similarly, Fig. 5(c) shows the detected acoustic signal and the corresponding spectrum at different positions along the x direction, as marked with the red dots. It can be observed that, as the vortex rotates constantly at the center of the field, the acoustic signal should exhibit phase and amplitude alterations, yet the vortex signals emerge at nearly the same time, except that several cycles of the signal are coherently cancelled in the center. The spectrum in Fig. 5(c) is consistent with the z -direction results. Moreover, the bandwidth of the actual optoacoustic vortex should be much larger than that shown here, considering the limitation of the piezoelectric transducer bandwidth.

Based on the spectral analysis given in Figs. 5(b) and 5(c), it is apparent that the central frequency of the acoustic signals is above 3.5 MHz, and the frequency distribution of the signals slightly varies, according to their measured positions. By combining the observation of the propagation distance and the central area of the vortex, as shown in Fig. 4(a), it can be concluded that the vortex appears at a distance of about $5\text{--}8\lambda$ from the generation surface in the z direction, while in the x - y plane it has a central area dimension of about $2\text{--}3\lambda$. Generally, the above results demonstrate that the generated three-dimensional optoacoustic vortex field can be captured within the expected spatial range, with a high center of frequency exceeding 3.5 MHz. Actually, there are higher-frequency components in the generated vortex field, but these are difficult to capture with the present detection system. The frequency and pressure amplitude can be further promoted to enhance the capability of particle manipulation, and the optoacoustic vortices can be feasibly tuned by temporally and spatially modulating the laser and improving the optoacoustic conversion structure.

V. CONCLUSIONS

We proposed an optoacoustic scheme for generating ultrasonic vortices and demonstrated that the logarithmic spiral absorption surface was capable of forming

the expected vortex acoustic field with a high central frequency beyond 3.5 MHz. To achieve high-resolution detection and dynamic visualization of the excited vortex acoustic field, a three-dimensional parabolic focusing detection system was constructed, and experimental studies were conducted on the distribution characteristics and spatial range of the ultrasonic vortex field. Common characteristic features of the vortex were clearly observed in both the simulation results and the experimental results. It was also demonstrated that this method was feasible for effectively exciting high-frequency ultrasonic vortices with controllable topological charge, indicating that optoacoustic technology could provide a complementary approach to traditional methods for acoustic vortex generation, with the advantage of remote triggering and high frequency. It is expected to be applied in particle manipulation, ultrasound therapy, and imaging.

ACKNOWLEDGMENTS

This work is supported by the National Natural Science Foundation of China (Grants No. 11974186, No. 61975080, and No. 12204242), the Natural Science Foundation of Jiangsu Province (Grant No. BK20200070), and the Fundamental Research Funds for the Central Universities (Grant No. 020414380195).

-
- [1] S. L. Chen, Y. C. Chang, C. Zhang, J. G. Ok, T. Ling, M. T. Mihnev, T. B. Norris, and L. J. Guo, Efficient real-time detection of terahertz pulse radiation based on photoacoustic conversion by carbon nanotube nanocomposite, *Nat. Photonics* **8**, 537 (2014).
 - [2] V. G. Andreev, A. A. Karabutov, and A. A. Oraevsky, Detection of ultrawide-band ultrasound pulses in optoacoustic tomography, *IEEE Trans. Ultrason. Ferroelectr. Freq. Control* **50**, 1383 (2003).
 - [3] M. Diego, M. Gandolfi, A. Casto, F. M. Bellussi, F. Violla, A. Crut, S. Roddaro, M. Fasano, F. Vallee, N. Del Fatti, P. Maioli, and F. Banfi, Ultrafast nano generation of acoustic waves in water via a single carbon nanotube, *Photoacoustics* **28**, 100407 (2022).
 - [4] Y. Hou, J. S. Kim, S. Ashkenazi, S. W. Huang, L. J. Guo, and M. O'Donnell, Broadband all-optical ultrasound transducers, *Appl. Phys. Lett.* **91**, 073507 (2007).
 - [5] Q. Li, J. Li, H. Zhu, Y. Chen, B. Zhu, and H. Yu, Dynamic acoustic focusing in photoacoustic transmitter, *Photoacoustics* **21**, 100224 (2021).
 - [6] I. Steinberg, D. M. Huland, O. Vermesh, H. E. Frostig, W. S. Tummers, and S. S. Gambhir, Photoacoustic clinical imaging, *Photoacoustics* **14**, 77 (2019).
 - [7] H. W. Baac, J. G. Ok, T. Lee, and L. J. Guo, Nanostructural characteristics of carbon nanotube-polymer composite films for high-amplitude optoacoustic generation, *Nanoscale* **7**, 14460 (2015).

- [8] B. Y. Hsieh, J. Kim, J. Zhu, S. Li, X. Zhang, and X. Jiang, A laser ultrasound transducer using carbon nanofibers–polydimethylsiloxane composite thin film, *Appl. Phys. Lett.* **106**, 021902 (2015).
- [9] L. H. V. Wang and S. Hu, Photoacoustic tomography: *In vivo* imaging from organelles to organs, *Science* **335**, 1458 (2012).
- [10] X. Du, J. Li, G. Niu, J. H. Yuan, K. H. Xue, M. Xia, W. Pan, X. Yang, B. Zhu, and J. Tang, Lead halide perovskite for efficient optoacoustic conversion and application toward high-resolution ultrasound imaging, *Nat. Commun.* **12**, 3348 (2021).
- [11] C. Tian, M. L. Pei, K. Shen, S. D. Liu, Z. M. Hu, and T. Feng, Impact of System Factors on the Performance of Photoacoustic Tomography Scanners, *Phys. Rev. Appl.* **13**, 014001 (2020).
- [12] Y. Jiang, H. J. Lee, L. Lan, H. A. Tseng, C. Yang, H. Y. Man, X. Han, and J. X. Cheng, Optoacoustic brain stimulation at submillimeter spatial precision, *Nat. Commun.* **11**, 881 (2020).
- [13] Y. Li, Y. Jiang, L. Lan, X. Ge, R. Cheng, Y. Zhan, G. Chen, L. Shi, R. Wang, N. Zheng, C. Yang, and J. X. Cheng, Optically-generated focused ultrasound for noninvasive brain stimulation with ultrahigh precision, *Light: Sci. Appl.* **11**, 321 (2022).
- [14] M. D. Brown, D. I. Nikitichev, B. E. Treeby, and B. T. Cox, Generating arbitrary ultrasound fields with tailored optoacoustic surface profiles, *Appl. Phys. Lett.* **110**, 094102 (2017).
- [15] W. Chan, T. Hies, and C. D. Ohi, Laser-generated focused ultrasound for arbitrary waveforms, *Appl. Phys. Lett.* **109**, 174102 (2016).
- [16] K. Passler, R. Nuster, S. Gratt, P. Burgholzer, and G. Paltauf, Laser-generation of ultrasonic *X*-waves using axicon transducers, *Appl. Phys. Lett.* **94**, 041101 (2009).
- [17] X. Jiang, D. A. Ta, and W. Q. Wang, Modulation of Orbital-Angular-Momentum Symmetry of Nondiffractive Acoustic Vortex Beams and Realization Using a Metasurface, *Phys. Rev. Appl.* **14**, 034014 (2020).
- [18] S. W. Fan, Y. F. Wang, L. Y. Cao, Y. F. Zhu, A. L. Chen, B. Vincent, B. Assouar, and Y. S. Wang, Acoustic vortices with high-order orbital angular momentum by a continuously tunable metasurface, *Appl. Phys. Lett.* **116**, 163504 (2020).
- [19] X. Jiang, Y. Li, B. Liang, J. C. Cheng, and L. Zhang, Convert Acoustic Resonances to Orbital Angular Momentum, *Phys. Rev. Lett.* **117**, 034301 (2016).
- [20] J. L. Thomas and R. Marchiano, Pseudo Angular Momentum and Topological Charge Conservation for Nonlinear Acoustical Vortices, *Phys. Rev. Lett.* **91**, 244302 (2003).
- [21] J. F. Nye and M. V. Berry, Dislocations in wave trains, *Proc. R. Soc. London, Ser. A* **336**, 165 (1974).
- [22] D. Baresch, J. L. Thomas, and R. Marchiano, Observation of a Single-Beam Gradient Force Acoustical Trap for Elastic Particles: Acoustical Tweezers, *Phys. Rev. Lett.* **116**, 024301 (2016).
- [23] A. Marzo, S. A. Seah, B. W. Drinkwater, D. R. Sahoo, B. Long, and S. Subramanian, Holographic acoustic elements for manipulation of levitated objects, *Nat. Commun.* **6**, 8861 (2015).
- [24] S. Jimenez-Gambin, N. Jimenez, and F. Camarena, Transcranial Focusing of Ultrasonic Vortices by Acoustic Holograms, *Phys. Rev. Appl.* **14**, 054070 (2020).
- [25] A. Marzo and B. W. Drinkwater, Holographic acoustic tweezers, *Proc. Natl. Acad. Sci. U. S. A.* **116**, 84 (2019).
- [26] L. Zhang and P. L. Marston, Angular momentum flux of nonparaxial acoustic vortex beams and torques on axisymmetric objects, *Phys. Rev. E* **84**, 065601 (2011).
- [27] P. L. Marston, Radiation force of a helicoidal Bessel beam on a sphere, *J. Acoust. Soc. Am.* **125**, 3539 (2009).
- [28] A. Marzo, M. Caleap, and B. W. Drinkwater, Acoustic Virtual Vortices with Tunable Orbital Angular Momentum for Trapping of Mie Particles, *Phys. Rev. Lett.* **120**, 044301 (2018).
- [29] X. Fan, Y. Zhu, Z. Su, N. Li, X. Huang, Y. Kang, C. Li, C. Weng, H. Zhang, W. Kan, and B. Assouar, Transverse Particle Trapping Using Finite Bessel Beams Based on Acoustic Metamaterials, *Phys. Rev. Appl.* **19**, 034032 (2023).
- [30] M. Baudoin, J. L. Thomas, R. A. Sahely, J. C. Gerbedoen, Z. Gong, A. Sivery, O. B. Matar, N. Smagin, P. Favreau, and A. Vlandas, Spatially selective manipulation of cells with single-beam acoustical tweezers, *Nat. Commun.* **11**, 4244 (2020).
- [31] Volke-Sepúlveda Karen, O. Arturo, Ricardo Santillán, and R. Boullosa, Transfer of Angular Momentum to Matter from Acoustical Vortices in Free Space, *Phys. Rev. Lett.* **100**, 24302 (2008).
- [32] Y. Li, G. Guo, J. Tu, Q. Ma, X. Guo, D. Zhang, and O. A. Sapozhnikov, Acoustic radiation torque of an acoustic-vortex spanner exerted on axisymmetric objects, *Appl. Phys. Lett.* **112**, 254101 (2018).
- [33] P. Q. Li, Z. L. Li, W. Zhou, S. W. Wang, L. Meng, Y. G. Peng, Z. Chen, H. R. Zheng, and X. F. Zhu, Generating Multistructured ultrasound via bioinspired metaskin patterning for low-threshold and contactless control of living organisms, *Adv. Funct. Mater.* **32**, 2203109 (2022).
- [34] Y. Fu, Y. Tian, X. Li, S. Yang, Y. Liu, Y. Xu, and M. Lu, Asymmetric Generation of Acoustic Vortex Using Dual-Layer Metasurfaces, *Phys. Rev. Lett.* **128**, 104501 (2022).
- [35] X. Xia, Y. Li, F. Cai, H. Zhou, T. Ma, J. Wang, J. Wang, and H. Zheng, Three-dimensional spiral motion of microparticles by a binary-phase logarithmic-spiral zone plate, *J. Acoust. Soc. Am.* **150**, 2401 (2021).
- [36] D. C. Chen, Q. X. Zhou, X. F. Zhu, Z. Xu, and D. J. Wu, Focused acoustic vortex by an artificial structure with two sets of discrete Archimedean spiral slits, *Appl. Phys. Lett.* **115**, 083501 (2019).
- [37] N. Jiménez, V. Romero-García, L. M. García-Raffi, F. Camarena, and K. Staliunas, Sharp acoustic vortex focusing by Fresnel-spiral zone plates, *Appl. Phys. Lett.* **112**, 204101 (2018).
- [38] J. Cao, K. Yang, X. Fang, L. Guo, Y. Li, and Q. Cheng, Holographic tomography of dynamic three-dimensional acoustic vortex beam in liquid, *Appl. Phys. Lett.* **119**, 143501 (2021).
- [39] S. W. Fan, S. D. Zhao, A. L. Chen, Y. F. Wang, B. Assouar, and Y. S. Wang, Tunable Broadband Reflective Acoustic Metasurface, *Phys. Rev. Appl.* **11**, 044038 (2019).
- [40] B. Assouar, B. Liang, Y. Wu, Y. Li, J. C. Cheng, and Y. Jing, Acoustic metasurfaces, *Nat. Rev. Mater.* **3**, 460 (2018).

- [41] T. Wang, M. Ke, W. Li, Q. Yang, C. Qiu, and Z. Liu, Particle manipulation with acoustic vortex beam induced by a brass plate with spiral shape structure, *Appl. Phys. Lett.* **109**, 123506 (2016).
- [42] Jiang Xue, Zhao Jiajun, Liu Shi-lei, Liang Bin, and Zou Xin-ye, Broadband and stable acoustic vortex emitter with multi-arm coiling slits, *Appl. Phys. Lett.* **108**, 203501 (2016).
- [43] S. Gspan, A. Meyer, S. Bernet, and M. Ritsch-Marte, Optoacoustic generation of a helicoidal ultrasonic beam, *J. Acoust. Soc. Am.* **115**, 1142 (2004).
- [44] S. Mezil, K. Fujita, P. H. Otsuka, M. Tomoda, M. Clark, O. B. Wright, and O. Matsuda, Active chiral control of GHz acoustic whispering-gallery modes, *Appl. Phys. Lett.* **111**, 144103 (2017).
- [45] M. A. Ghanem, A. Khanolkar, H. Zhao, and N. Boechler, Nanocontact tailoring via microlensing enables giant post-fabrication mesoscopic tuning in a self-assembled ultrasonic metamaterial, *Adv. Funct. Mater.* **30**, 144103 (2020).
- [46] Y. Jin, R. Kumar, O. Poncelet, O. Mondain-Monval, and T. Brunet, Flat acoustics with soft gradient-index metasurfaces, *Nat. Commun.* **10**, 143 (2019).
- [47] B. E. Treeby and B. T. Cox, *k*-Wave: MATLAB toolbox for the simulation and reconstruction of photoacoustic wave fields, *J. Biomed. Opt.* **15**, 021314 (2010).
- [48] Z. Chen, Y. Wu, Y. Yang, J. Li, B. Xie, X. Li, S. Lei, J. Ouyang, X. Yang, Q. Zhou, and B. Zhu, Multilayered carbon nanotube yarn based optoacoustic transducer with high energy conversion efficiency for ultrasound application, *Nano Energy* **46**, 314 (2018).